Article

18Ni300 Maraging Steel Lattice Structures Fabricated via Laser Powder Bed Fusion—Mechanical Behavior and Gas Permeability

D. F. Oliveira [1,2], J. S. Vieira [3,4], I. Duarte [5,6], G. Vincze [5], J. M. Oliveira [1,3,4] and G. Miranda [1,2,*]

1   CICECO, Aveiro Institute of Materials, University of Aveiro, 3810-193 Aveiro, Portugal;
     diogo.olive@ua.pt (D.F.O.); martinho@ua.pt (J.M.O.)
2   Department of Materials and Ceramic Engineering (DEMaC), University of Aveiro, 3810-193 Aveiro, Portugal
3   EMaRT, Emerging Materials and Research Technologies, University of Aveiro, 3810-193 Aveiro, Portugal
4   School of Design, Management and Production Technologies Northern Aveiro, University of Aveiro,
     3720-509 Oliveira de Azeméis, Portugal
5   Department of Mechanical Engineering, Centre for Mechanical Technology and Automation (TEMA),
     University of Aveiro, 3810-193 Aveiro, Portugal; isabel.duarte@ua.pt (I.D.); gvincze@ua.pt (G.V.)
6   LASI—Intelligent Systems Associate Laboratory, 4800-058 Guimarães, Portugal
*   Correspondence: gmiranda@ua.pt

Abstract: Maraging steels have attracted the attention of the injection molding industry, mainly due to their mechanical properties. However, the use of these steels for complex inserts is still a challenge, given the limitations of conventional subtractive technologies. In this context, additive manufacturing technologies, especially Laser powder bed fusion (LPBF), arise as a solution for the manufacture of maraging steel parts with innovative designs. In this study, 18Ni300 maraging steel lattice structures with different architectures were designed and manufactured via Selective Laser Melting (SLM), targeting mold vents for gas escape during injection molding. Three types of structures, simple cubic (SC), body-centered cubic (BCC), and gyroid (G), with different dimensions were produced, and their mechanical performance under compression (prior and after aging treatment) and gas permeability were investigated. The produced structures displayed a first maximum compressive strength from 54.3 to 251.5 MPa and an absorbed energy (up to 0.5 strain) between 34.8 and 300.6 MJ/m^3. After aging, these properties increased, with the first maximum compressive strength ranging from 93.0 to 453.3 MPa and the absorbed energy ranging from 34.8 to 300.6 MJ/m^3. The SC structures' permeability was found to be between 4.9×10^{-11} and 2.0×10^{-10} m^2, while for the BCC structures, it was between 2.2×10^{-11} and 1.2×10^{-10} m^2. The gyroid structures' permeability ranged from 6.7×10^{-11} to 1.6×10^{-10} m^2. This study shows that a tailored permeability can be attained through the design of AM lattice structures, via different architectures, that assure distinct mechanical properties.

Keywords: 18Ni300; maraging steel; selective laser melting; lattice structures; permeability

1. Introduction

Lattice structures are used today in a variety of fields, from electronics to aerospace, aiming to significantly change properties and maximize performance. Applications span from sound absorption and heat dissipation materials to crash energy absorbers and biomedical devices, as lattice structures are viable solutions to obtain adequate combinations of properties while reducing energy usage, material waste, and fabrication time, especially when additive manufacturing is used [1,2].

Lattice structures are composed of unit cells that are continuously repeated, thus having a periodic nature [3]. A broad range of lattice structures with very distinctive unit cells, from cubic or body-centered cubic to more complex structures such as triply periodic minimal surface (TPMS), can be found in several studies, frequently to reduce weight, increase specific strength, or modulate stiffness [4]. In fact, the biomedical field has prompted the use of lattice structures, particularly for reducing load-bearing implants'

stiffness to values closer to those of bone [5] or to allow body fluids to flow through these structures [6]. Gyroids are TPMS structures composed of continuous and smooth shells, allowing a high surface/volume ratio and high interconnectivity. These structures are expressed by a mathematical function that defines the regular and smooth geometries without discontinuities [7].

The maturity of additive manufacturing (AM) technologies for metallic material fabrication is allowing the consolidation of these structures' integration into conventionally designed systems. Powder bed fusion (PBF) and Directed Energy Deposition (DED) are the most effective AM processes for metal and alloy fabrication among those detailed in ISO 17296-2:2015 [8], with PBF granting a higher precision and accuracy for the fabrication of thin-walled parts [9]. PBF technologies use powder bed layer-by-layer fabrication, where defined areas are sintered (Selective Laser Sintering (SLS)) or melted (Selective Laser Melting (SLM) or Electron Beam Melting (EBM)), using a laser (SLM and SLS) or an electron beam (EMB) as the energy source [10]. Laser powder bed fusion's ability to produce parts with complex geometries without the use of tools or molds, together with its capacity to fabricate materials with high mechanical properties given the high densification (99.5% in metals and alloys) [11], makes LPBF technologies like Selective Laser Melting suitable for lattice structure fabrication, as previous examples have demonstrated [12–14]. From a sustainability point of view, it is important to highlight the high recyclability of powdered materials [15] besides the flexibility of these technologies for changes in product design [3,9,15]. However, laser powder bed fusion (LPBF) is a highly dynamic and complex process combining several physical phenomena; thus, during fabrication, it is highly beneficial to assess the relationships between laser energy density, melt flow, and plume and spattering behavior as these will dictate the number and severity of defects on the fabricated parts. Wang You et al. [16] effectively monitored in situ and recorded in real time the plume and spattering behavior based on image recognition, and then optimized the process parameters to promote process stability and reduce defects.

Maraging steels are martensitic steels that typically undergo age hardening, a heat treatment usually performed at temperatures between 455 and 510 °C over several hours, in order to promote the precipitation of fine intermetallic compounds within the alloy [17,18]. Some examples of these precipitates are Ni_3Ti, Ni_3Mo, Ni_3Al, and Fe_2Mo, but their presence and amount are dependent on the aging time and temperature [19]. These alloys with low carbon content exhibit very high mechanical strength and hardness due to the precipitation of these intermetallic compounds during the age hardening, while also displaying high toughness, good weldability, and high dimensional stability [17,20]. Due to these properties, maraging steels are commonly used in machining tools [21], molds [6], and high-strength components [22].

Metallic lattice structures have been explored for the injection molding industry, either by tailoring fluid flow for internal cooling [23], for heat sinks [24] or mold venting [25,26], or for assuring the required specific strength and lowering the weight of molding systems [3]. The work by Davar Ali et al. [27] demonstrates that by designing different gyroid and rectangular-pore lattices, it is possible to tailor permeability. A study from S. Ma et al. [28] shows that SLM is an efficient technology to fabricate 316L steel lattice structures with the desired permeability and mechanical properties, while A. Dhinakar et al.'s [29] work shows that SLM processing parameters significantly influence the permeability of the fabricated lattice structures, as the processing parameters dictate these structures' dimensional and geometrical accuracy. A widespread industrial solution for injection mold gas venting is the use of commercially available porous inserts, commonly sintered metals, that are assembled in the molding system. AM can bring improved performance to these parts as it allows the fabrication of thin-walled and structured parts with customized permeability, suited for a specific mold. The possibility to fabricate accurately controlled structures inside mold inserts that have any outer geometry is a competitive advantage of LPBF technologies like SLM. Moreover, it allows great flexibility for developing and producing inserts for

increasingly complex molding systems, which are not possible using commercial simple geometry vents.

This study addresses three different 18Ni300 maraging steel lattice structures, two strut-based (simple cubic (SC) and body-centered cubic (BCC)) and a TPMS (gyroid (G)), that were designed and subsequently manufactured via SLM, aiming at their incorporation in mold vents for gas escape during the injection process. This study brings valued information for the design of AM porous vents for injection molding applications, with a tailored combination of permeability and mechanical properties.

2. Experimental Procedure

2.1. Materials and SLM Fabrication Details

For the lattice structures' fabrication, 18Ni300 maraging steel gas-atomized powder (from RENISHAW, Wotton-under-Edge, UK) was used, which composed of nearly spherical particles (see Figure 1) as presented in Table 1. This feedstock particle size distribution was experimentally assessed using HORIBA Scientific—LA—960V2 (HORIBA, Tokyo, Japan) which can be seen in Figure 1 (right), revealing a D_{50} = 33 μm and D_{90} = 44 μm.
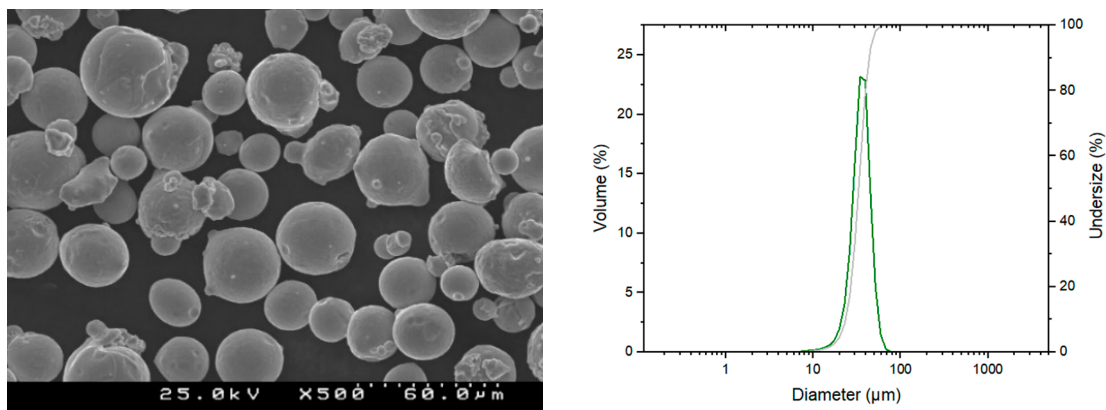

Figure 1. 18Ni300 maraging steel powder: SEM image (**left**) and particle size distribution (**right**).

Prior to the SLM fabrication, the flowability of the powder was evaluated via the Hall funnel method following ASTM B213-20 [30], with a flow rate (s/50 g) of 38.2 ± 0.4 being experimentally determined.

Table 1. 18Ni300 maraging steel powder composition, according to the manufacturer (data from Ref. [31]).

Element	Ni	Co	Mo	Ti	C	Others
wt. (%)	17 to 19	7 to 10	4.5 to 5.2	0.3 to 1.2	≤0.03	Bal.

The lattice structures were manufactured on an SLM apparatus from RENISHAW, model RenAM 500Q, equipped with four 500 W lasers with a spot size of 80 μm. The set of parameters used for the fabrication is found in Table 2 and was previously assessed in a previous work [32].
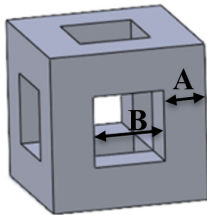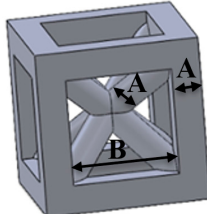
Three types of lattice structures were designed using 3D CAD software (Dassault Systèmes-SolidWorks Corporation, Waltham, MA, USA), two strut-based lattice structures (simple cubic (SC) and body-centered cubic, in which the unit cell has inner circular section struts and horizontal and vertical square section struts (BCC)) and one triply periodic minimal surface (TPMS) lattice structure (gyroid (G)).

Table 2. Process parameters used for the lattice structures' SLM fabrication.

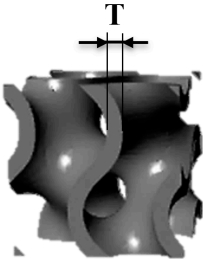| Parameter	Value
Laser power (P)	250 W
Scanning speed (v)	1000 mm/s
Hatch distance (d)	75 μm
Layer thickness (t)	50 μm
Build plate temperature (T)	170 °C
Volumetric energy density (E)	54.14 J/mm^3

Table 3 shows the designed unit cells of the SC and BCC structures, indicating the struts' (A) and pores' (B) dimensions. For the fabrication of the cuboid specimens with edges between 15.3 and 15.9 mm, the number of unit cells was accordingly adjusted to the necessary integer.

Table 3. SC and BCC structures' unit cell CAD dimensions and corresponding specimen CAD porosity.

Structure		A (μm)	B (μm)	Porosity (%)
	SC300		300	48.53
	SC400		400	59.04
	SC500	300	500	66.64
	SC600		600	72.33
	SC700		700	76.66
	BCC700		700	50.69
	BCC800		800	57.06
	BCC1000	300	1000	66.74
	BCC1100		1100	70.43
	BCC1200		1200	73.53

The gyroid structures' details are indicated in Table 4, namely the strut dimension (T), the number of unit cells per specimen, and the resulting CAD porosity.

Table 4. Gyroid structures' unit cell CAD dimensions and corresponding specimen CAD porosity.

Structure		T (μm)	Number of Unit Cells	Porosity (%)
	G700	700		54.06
	G600	600		60.76
	G500	500	3	67.38
	G400	400		73.95
	G300	300		80.43

2.2. Post-Fabrication Heat Treatment

After being removed from the build plate, the structures underwent precipitation hardening heat treatment. The samples were placed in a furnace, heated at a rate of 242 °C/h up to a temperature of 510 °C, and kept for six hours under an argon atmosphere. The samples were allowed to cool inside the furnace until they reached room temperature.

2.3. Characterization and Testing

2.3.1. Lattice Structures' Characterization

SEM images and micro-CT analysis were used to assess the fabricated structures' general quality in terms of the presence of macro- and micro-defects, substantive deviations in the CAD design, or minor differences regarding the structures' dimensions, namely the strut diameter or thickness and pore size. A micro-CT scanner (Bruker SkyScan X-ray microtomograph 1275, Billerica, MA, USA) was used to scan two structures per group, both at 11 μm resolution and using 80 kV voltage.

In addition, starting from mass measurement and using the density of 18Ni300 maraging steel (8.1 g/cm^3 [31]), the porosity was determined for each sample for a comparison with the CAD porosity.

2.3.2. Phase Identification and Microstructure

X-ray diffraction (XRD) was performed using a Panalytical/X'Pert PRO^3 (Panalytical, Almelo, Netherlands) equipped with a Cu-Ka radiation source to examine the crystalline phases of the SLM-fabricated steel. XRD patterns were obtained using a step size of 0.02° in the 2θ range from 20 to 90°. The polished surface of the 18Ni300 samples was etched with a solution of nitric acid (HNO_3) and ethanol (15% vol% Nital) for 15 s to observe the microstructure through an optical microscope (Jenaphot^{2000}, Carl Zeiss, Oberkochen, Germany).

2.3.3. Compression Tests

Compression tests were performed on a Shimadzu AG-25TA apparatus according to ISO 13314:2011 [33], using a 0.9 mm/min speed up to 0.6 strain. Static compression without lubrication was performed with no lateral constraining of the samples, applying the load in the samples' building direction. At least five tests were performed to ensure reproducibility and to calculate average values.

Following ISO 13314:2011, several properties were determined, namely the quasi-elastic gradient, corresponding to the gradient of the straight line determined within the linear deformation region at the beginning of the compressive stress–strain curve; the first maximum compressive strength, corresponding to the first local maximum in the stress–strain curve; and the energy absorption (W), corresponding to the area under the stress–strain curve up to 0.5 strain.

2.3.4. Permeability Tests

Regarding permeability tests, special specimens were built via SLM for perfectly fitting an in-house-developed permeability apparatus, as depicted in Figure 2. Specimens with an outer diameter of 7.2 mm and an inner architecture as described in Tables 3 and 4 were produced (SC, BCC, and gyroid). Five different pressure differences were tested, namely 0.5; 1.0; 1.5; 2.0; and 2.5 bar. The permeability results presented herein are an average of a minimum of three measurements, made in three different samples, per group.
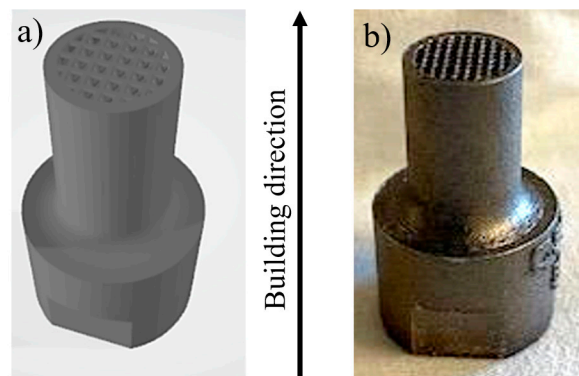
Figure 2. CAD design (**a**) and SLM-fabricated (**b**) specimen for permeability test.

3. Results and Discussion

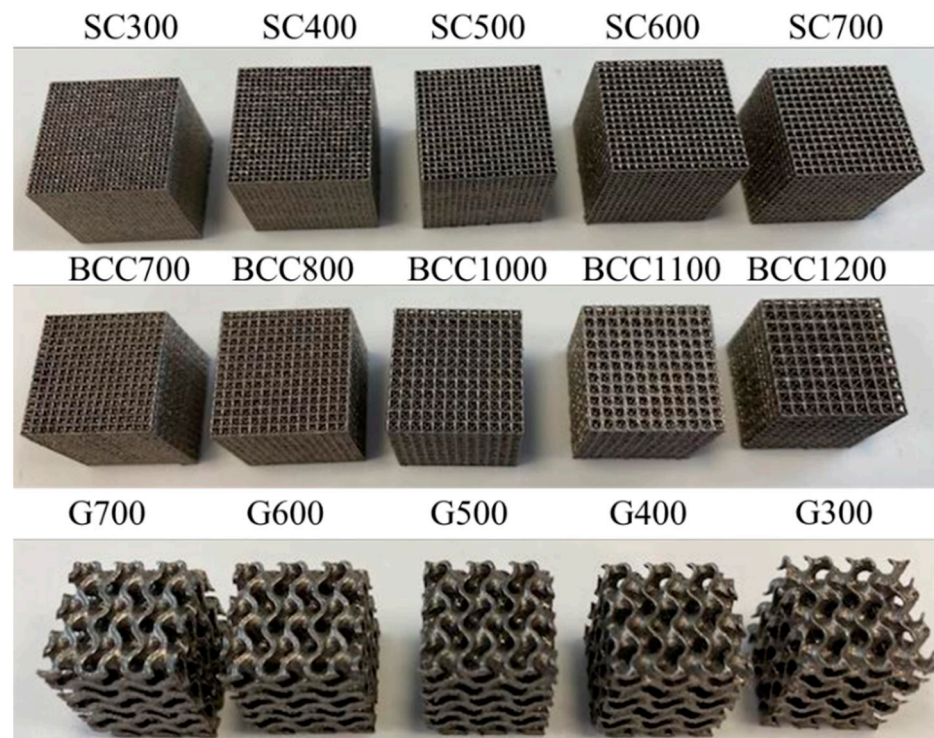Figure 3 shows images of the SLM-fabricated specimens from the different experimental groups.
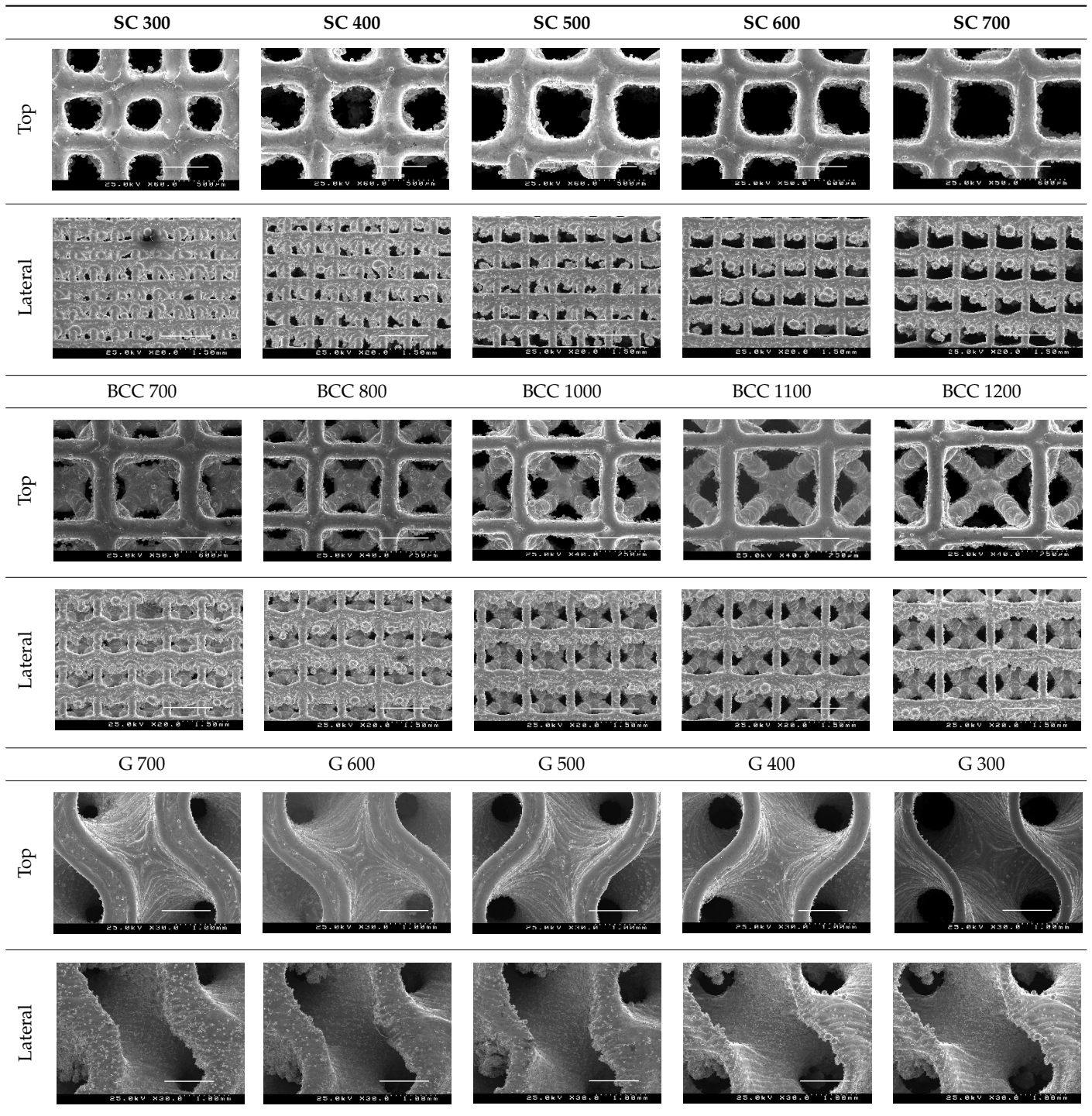

Figure 3. Simple cubic (SC), body-centered cubic (BCC), and gyroid (G) lattice structures manufactured via SLM.

3.1. Morphological and Dimensional Characterization

Table 5 shows the top and lateral surfaces of specimens from each experimental group, allowing one to perceive the presence of partially molten particles at the structures' struts. This effect is more pronounced in the lateral surfaces, as these are more exposed to loose powder during the SLM incremental process, than the top surface. In addition, some non-melted powder can be found inside the structures, even after compressed air and ultrasonic cleaning, especially in the SC and BCC structures, which have the smallest pore size.

Table 5. Top and lateral images for all the experimental groups.

	SC 300	SC 400	SC 500	SC 600	SC 700
Top					
Lateral					
	BCC 700	BCC 800	BCC 1000	BCC 1100	BCC 1200
Top					
Lateral					
	G 700	G 600	G 500	G 400	G 300
Top					
Lateral					

MicroCT analysis (Figure 4) shows that the produced structures do not exhibit constructive defects but instead substantiate the analysis made via SEM, regarding the geometrical accuracy of the technology for obtaining these architectured specimens.

The fabricated structures' porosity was assessed and compared with the corresponding CAD porosity (Table 6).
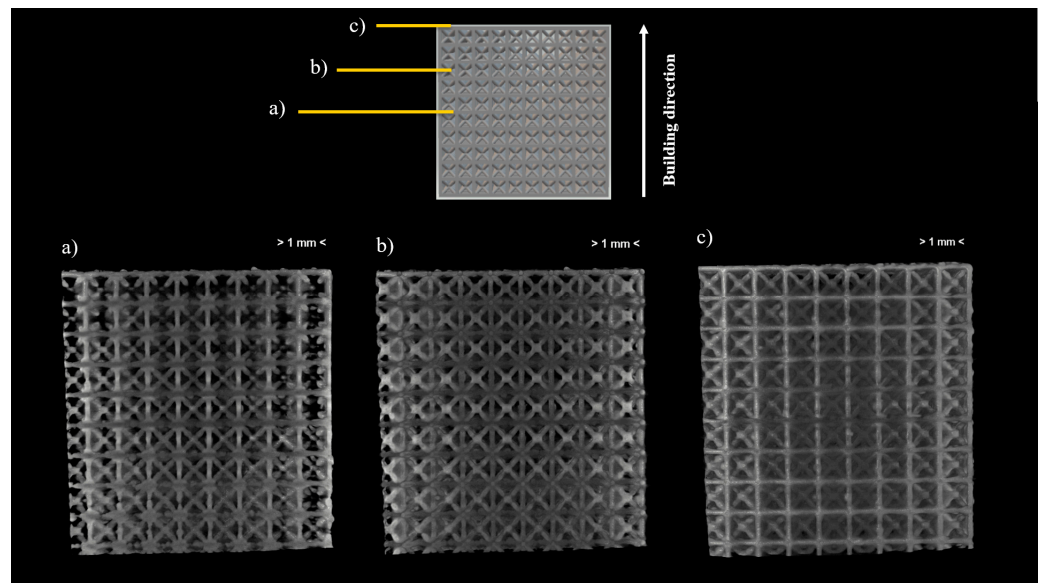
Figure 4. Multipoint μCT images of BCC1200 specimen. Multipoint Uct images of BCC1200 specimen (sections a, b and c))

Table 6. CAD and experimental porosity for SC, BCC, and gyroid groups.

| Structure | Porosity (%) | | | |
| | CAD | Experimental | | % Difference (Exp.-CAD) |
		Average	S.D.	
SC300	48.53	45.77	0.89	−5.7%
SC400	59.04	54.50	0.41	−7.7%
SC500	66.64	61.48	0.84	−7.7%
SC600	72.33	68.14	0.45	−5.8%
SC700	76.66	72.44	0.33	−5.5%
BCC700	50.69	42.55	0.67	−16.1%
BCC800	57.06	50.58	0.52	−11.4%
BCC1000	66.74	60.99	0.47	−8.6%
BCC1100	70.43	65.37	0.53	−7.2%
BCC1200	73.53	68.42	0.71	−6.9%
G700	54.06	55.11	0.12	1.9%
G600	60.76	61.69	0.12	1.5%
G500	67.38	68.41	0.18	1.5%
G400	73.95	74.02	0.10	0.1%
G300	80.43	79.88	0.09	−0.7%

When analyzing the strut-based structures (SC and BCC), it was consistently observed that, in all groups, the experimental porosity was lower than the CAD porosity. This difference was mainly due to the partially melted powder, which reduced the structures' open-cell size, as seen in the micro-CT reconstruction (Figure 4) and SEM images in Table 5, and some entrapped powder. This experimentally determined reduction in porosity was higher for the BCC structures than the SC ones, as the former have more struts where partially melted powder can be found. Regarding gyroid structures, much lower deviations in the CAD porosity were observed, showing a higher reproducibility in this case.

3.2. Phase Identification and Microstructure

The XRD spectra obtained for 18Ni300 maraging steel, after SLM fabrication and after heat treatment, are shown in Figure 5. The XRD analysis performed after SLM fabrication revealed three peaks at 44.30°, 64.35°, and 81.73°, corresponding to the martensitic phase. After the heat treatment, the previously mentioned peaks were also detected, confirming the presence of martensite, but in addition, peaks corresponding to intermetallic compounds (Fe_2Mo and FeTi) were also detected, as well as one peak corresponding to the austenitic phase (γ). The precipitation of intermetallic compounds in maraging steel originates due to heat treatment inducing nickel enrichment in the matrix, decreasing the transformation temperature of the martensite phase to austenite, and thus favoring the stability of austenite. Consequently, the amount of retained austenite increases during the heat treatment [34]. Several intermetallics are reported in the literature as being formed during SLM 18Ni300 steel aging treatments, with these being commonly reported Fe_2Mo and Ni_3Ti [35,36].
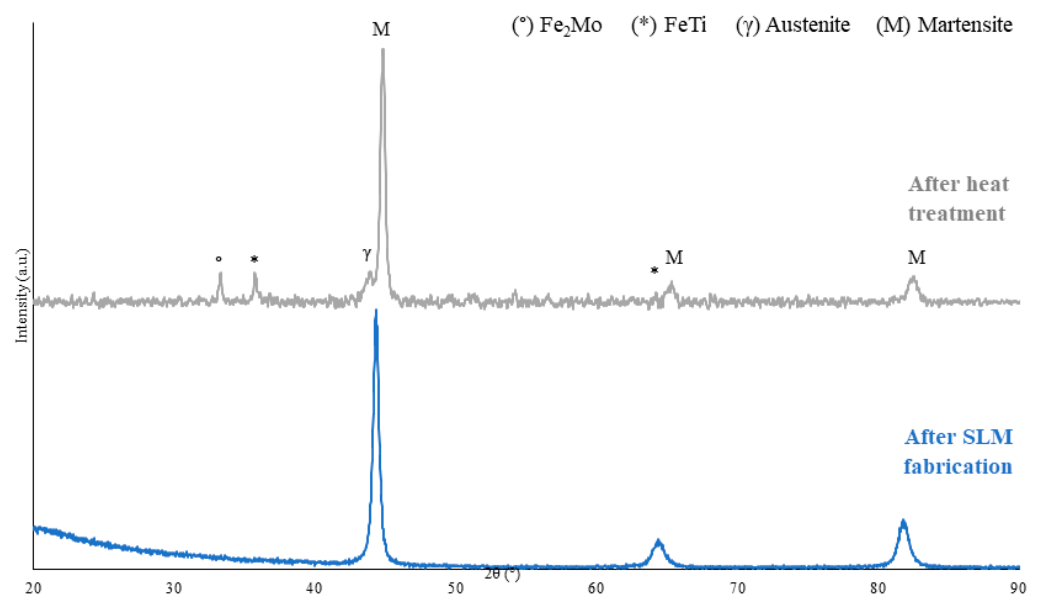

Figure 5. XRD spectra of SLM 18Ni300 maraging steel before and after heat treatment.

Figure 6 depicts cross-section images showing this steel microstructure before and after heat treatment. Figure 6a shows a cell microstructure typical of 18Ni300 maraging steels, as fabricated via SLM. The cells have a dimension of approximately 0.20 to 0.45 μm, within the expected range when fabricated by SLM [34,37]. The cellular structure is caused by microsegregation during the solidification process, which results in the enrichment of some alloying elements (Ni) in the interdendritic regions [37]. The resulting structure consists of martensite inside the cells and residual austenite retained along the grain boundaries [37]. Figure 6b shows the microstructure after heat treatment, with a less defined cell microstructure, as described by Bai et al. [38]. Nanoprecipitates were detected in previous studies addressing the SLM fabrication of maraging steels [39], and these are commonly reported to be diffusely distributed at the martensite grain boundaries and inside the martensite grains [36].
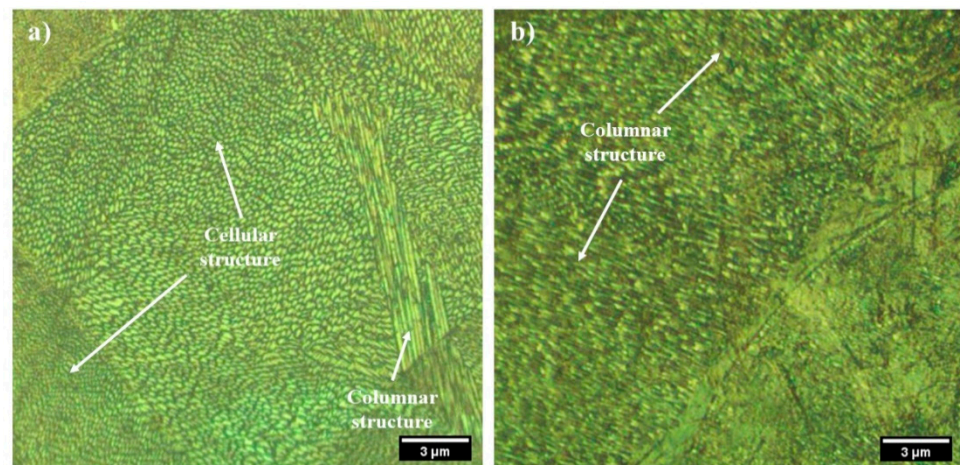
Figure 6. SLM 18Ni300 microstructure (**a**) before and (**b**) after heat treatment.

3.3. Mechanical Testing

Figure 7 shows representative curves for each group of structures, showing that similar compressive behavior was perceived among the same type of structures, albeit achieving different stress magnitudes.
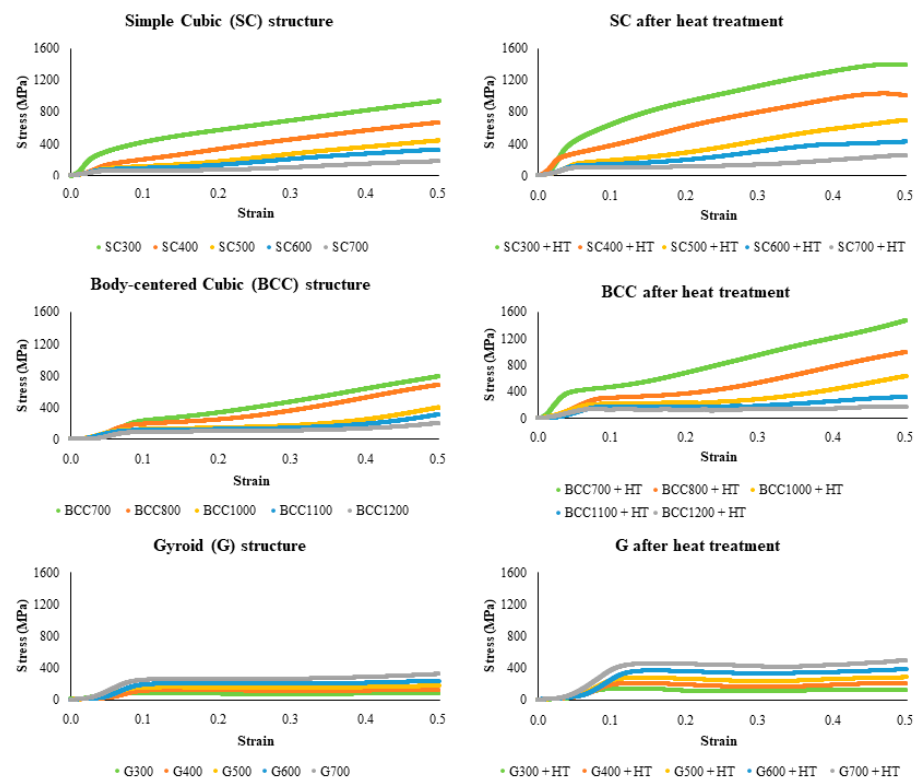

Figure 7. Representative stress–strain curves for each group of structures.

Figure 8 shows representative stress–strain curves corresponding to structures with intermediate dimensions in each experimental group (simple cubic (SC500), body-centered cubic (BCC1000), and gyroid (G500) structures). Also, in Figure 8, there are images captured at identified moments in the stress–strain curve, which allow understanding the compaction phenomena during compression in the different types of structures. When comparing the different types of structures, evident plateau stresses are displayed in the gyroid and BCC structures, although they are less pronounced in the latter.
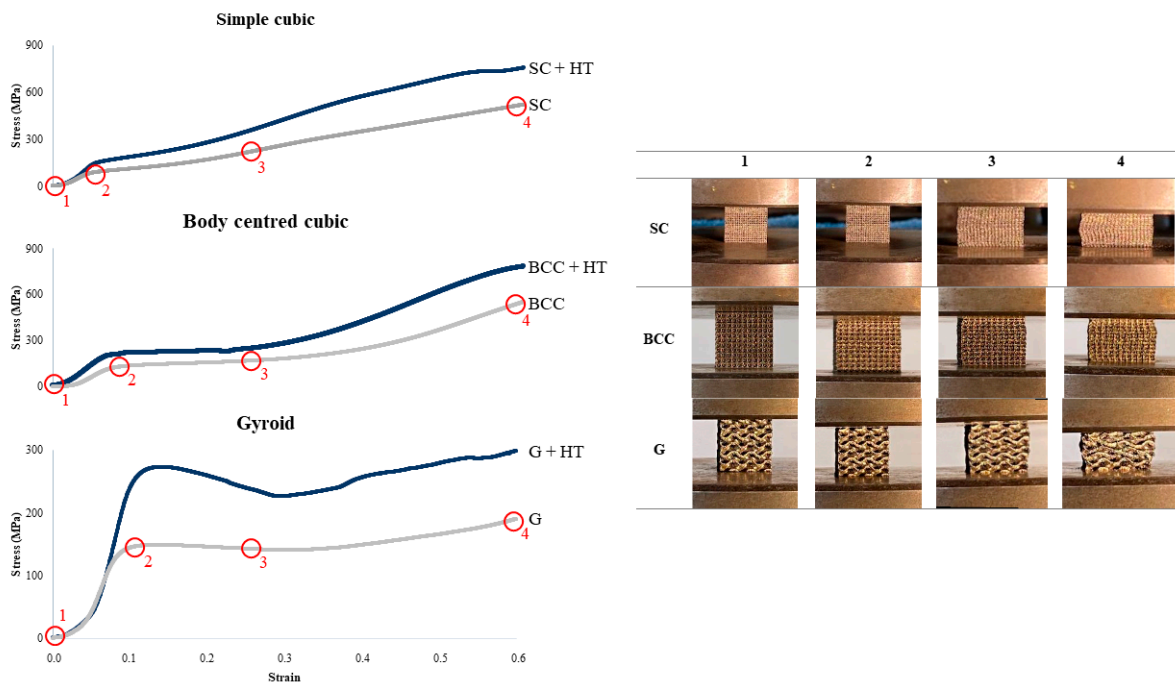
Figure 8. Stress–strain curves of representative samples of each type of structure before and after heat treatment and images captured at identified moments.

The curves obtained show similar behavior to that found in the literature, such as in the studies by S. Ma et al. and Y. Chen et al. [28,40], and according to the ISO 13314:2011 standard. The obtained curves show a gradual collapse of the structures as no sudden stress variations are perceived.

3.3.1. First Maximum Compressive Strength

From the experimentally obtained curves, the first maximum compressive strength was determined, with Figure 9 depicting the average values for all the tested structures with different dimensions and architectures.
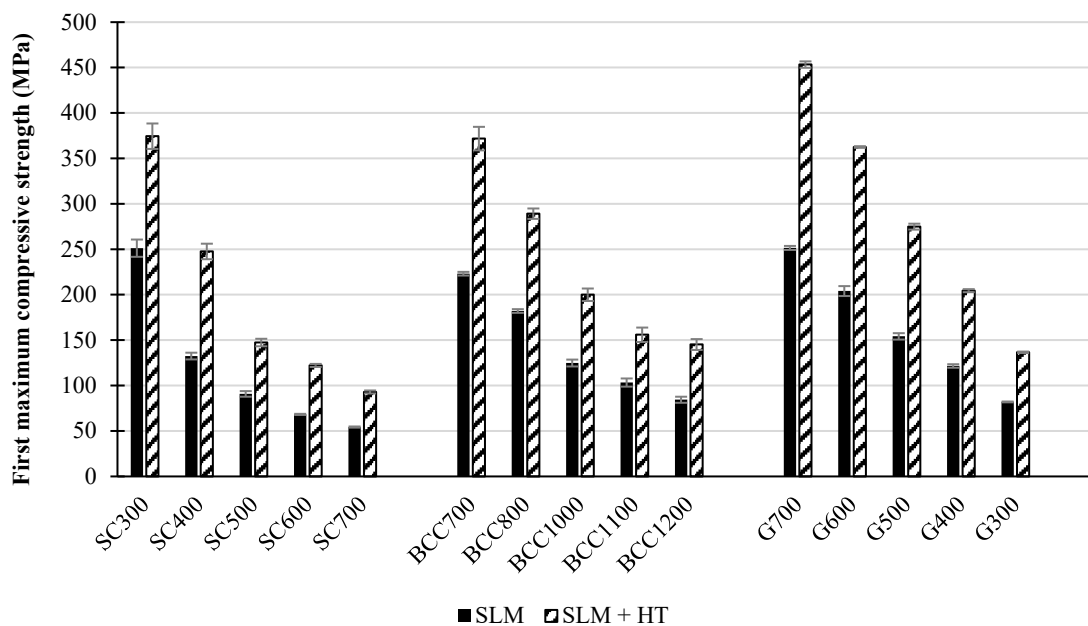

Figure 9. First maximum compressive strength of SC, BCC, and gyroid structures.

Overall, the structures fabricated in this study displayed a first maximum compressive strength between 54.3 (±0.7) and 251.5 (±2.3) MPa (before heat treatment) and between 93.0 (±1.7) and 453.3 MPa (±3.6) (after heat treatment).

As expected, increasing the SC and BCC structures' pore size led to significant decreases in compressive strength for the as-produced structures (SLM in Figure 9) as well as for the heat-treated structures (SLM + HT in Figure 9). When comparing SC700 with SC300, there was a decrease of approximately 78%. For the BCC structures, a decrease of approximately 62% was verified when comparing BCC1200 with BCC700. The compressive strength ranges of the SC and BCC structures are quite distinct, since BCC structures have internal struts that impart higher mechanical strength. Taking SC700 and BCC700 structures after fabrication as examples, they have the same pore size yet exhibit a first maximum compressive strength of 54.3 (±0.7) MPa (SC) versus 223.1 (±2.1) MPa (BCC), corresponding to an significant 311% increase. Regarding the heat-treated structures, a very similar influence of pore size was verified, with decreases of 75% (SC700 when compared to SC300) and 61% (BCC1200 when compared to BCC700). Again, the first maximum compressive strengths of the SC700 and BCC700 structures were compared, this time after heat treatment, and an increase of 300% was verified, much in line with the results for these structures before heat treatment. As for the effect of the heat treatment in the strut-based structures, an average increase of 65.7% in the first maximum compressive strength was determined for all the tested structures of different dimensions.

The gyroid structures displayed a similar trend, with an increase in the first maximum compressive strength of approximately 207% with increasing strut dimension (T) when comparing G700 with G300 prior to heat treatment, corresponding to 251.5 (±2.3) and 82.0 (±0.4) MPa, respectively. Similarly, after heat treatment, an increase in compressive strength of approximately 232% was verified when comparing G700 to G300. Regarding the effect of the heat treatment on the gyroid structures, an average 74.2% increase in compressive strength was achieved by performing the heat treatment for all the tested structures of different dimensions. P. Bajaj et al. [37], D. Ferreira et al. [32], and K. Kempen et al. [41] compared the yield and tensile strength of solid 18Ni300 fabricated via SLM before and after heat treatment, reporting an average 73% increase in these properties after heat treatment, aligned with the increases determined in this study for the different architectures.

3.3.2. Quasi-Elastic Gradient

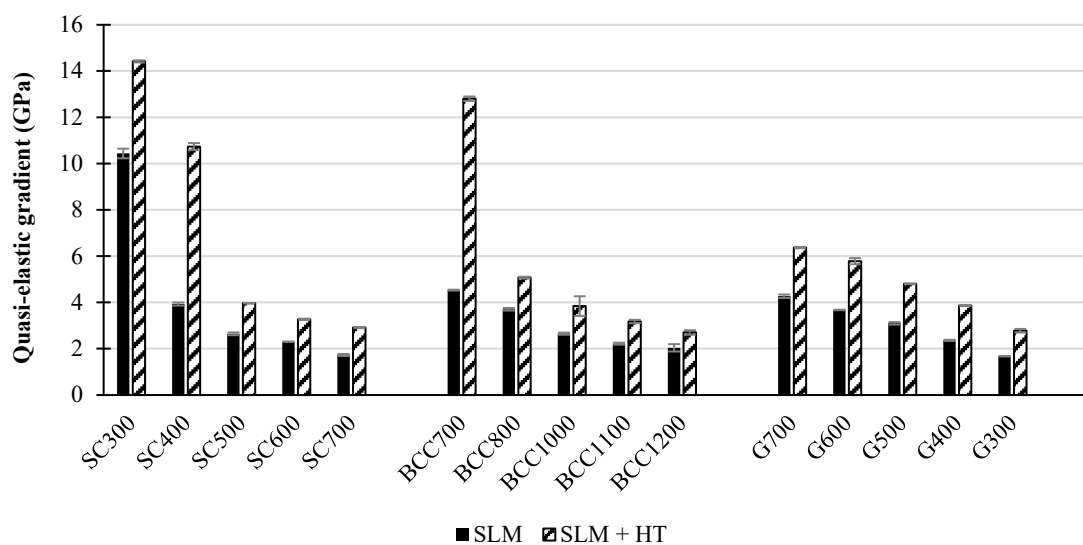Figure 10 shows the quasi-elastic gradient for all the tested structures with different dimensions and architectures.

Figure 10. Quasi-elastic gradient of SC, BCC, and gyroid structures.

It is known that the porosity of lattice structures can be tuned to achieve a given stiffness [28,40]. And while the modulus of elasticity of 18Ni300 maraging steel fabricated via powder bed fusion technologies ranges between 181 and 220 GPa before and after treatment, respectively [37], the structures fabricated in this study displayed a quasi-elastic gradient between 1.73 ($\pm$0.04) and 10.44 ($\pm$0.21) GPa (before heat treatment) and between 2.91 ($\pm$0.02) and 14.42 ($\pm$0.05) GPa (after heat treatment).

When analyzing the SC and BCC structures, this effect is clearly demonstrated, with higher pore sizes leading to a lower quasi-elastic gradient, both after fabrication and after heat treatment. Regarding the as-produced simple cubic structures, a decrease in the quasi-elastic gradient of 83% can be observed when comparing SC700 with SC300 (the lowest pore size in the SC group). Comparing the BCC structures BCC1200 to BCC700 (the lowest pore size in the BCC group), this decrease was 55%. The architecture differences between SC and BCC were responsible for the differences between SC700 and BCC700, which have equal pore size and strut diameter. These results are comparable to those reported by Y. Chen et al. [40], where moduli of elasticity between 2.1 GPa and 15.0 GPa, were reported for 316L BCC structures as-produced via SLM.

Regarding the SC and BCC structures after heat treatment, 80% and 79% decreases in the quasi-elastic gradient were found with increasing pore size, respectively. As for the effect of the heat treatment on structures with the same typology/dimensions, an increase between 68 and 75% in the quasi-elastic gradient was determined.

As for the gyroid structures, quasi-elastic gradients between 1.68 ($\pm$0.01) and 4.27 ($\pm$0.08) GPa (before heat treatment) and between 2.78 ($\pm$0.08) and 6.37 ($\pm$0.03) GPa (after heat treatment) were observed. With an increase in the strut dimension (T), there was an overall increase in the quasi-elastic gradient as expected. Comparing G700 with G300 before heat treatment, this increase was approximately 61%. A study conducted by S. Ma et al. [28] on 316L gyroid structures fabricated via SLM, with struts of 300, 400, and 500 μm, reported moduli of elasticity of 2.0 GPa, 2.5 GPa, and 2.7 GPa, respectively, which are comparable to those obtained in this study, where the strut dimension varied between 300 and 700 μm.

When comparing G300 to G700, decreases of 61% and 56% were observed before and after heat treatment, respectively. Overall, the heat treatment of the gyroid structures led to an increase in the quasi-elastic gradient from 57 to 59% for the various dimensions tested.

3.3.3. Energy Absorption (W)

A lattice structure's ability to combine light weight with energy absorption is a strategic advantage for several applications, including molding and tooling. From the stress–strain curves, it is possible to determine the energy absorption, corresponding to the area under the curve up to a given extension. In this study, the energy absorption was determined up to 0.5 strain, and the average values are presented in Figure 11.

Figure 11 shows that the SC and BCC structures displayed energy absorption between 49.37 ($\pm$2.20) and 300.56 ($\pm$8.80) MJ/m^3 (before heat treatment) and between 63.86 ($\pm$1.86) and 493.84 ($\pm$10.52) MJ/m^3 (after heat treatment). These strut-based structures display a clear trend, similar to what was previously discussed for compression strength, with higher pore size leading to lower absorbed energy. Regarding the structures before heat treatment, an 84% decrease in the absorbed energy occurred when increasing the porosity from 45.77% (SC300) to 72.44% (SC700). For the BCC structures, this decrease was 75% comparing BCC700 (42.55% porosity) with BCC1200 (68.42%). When comparing structures with equal pore size but different architectures, namely SC700 and BCC700, very different energy absorption values were achieved, namely 49.37 ($\pm$2.20) and 202.08 ($\pm$7.68) MJ/m^3, respectively, due to the lower porosity of BCC structures when compared to simple cubic ones (72.44% for SC700 versus 42.55% for BCC700). After treatment, similar decreases in the absorbed energy were verified when increasing the pore size (and consequently, the porosity). When comparing lower- and higher-porosity SC structures (SC300 and SC700), a

decrease of 86% in the absorbed energy was verified. For the BCC structures, this decrease was 84% (BCC1200 versus BCC700).
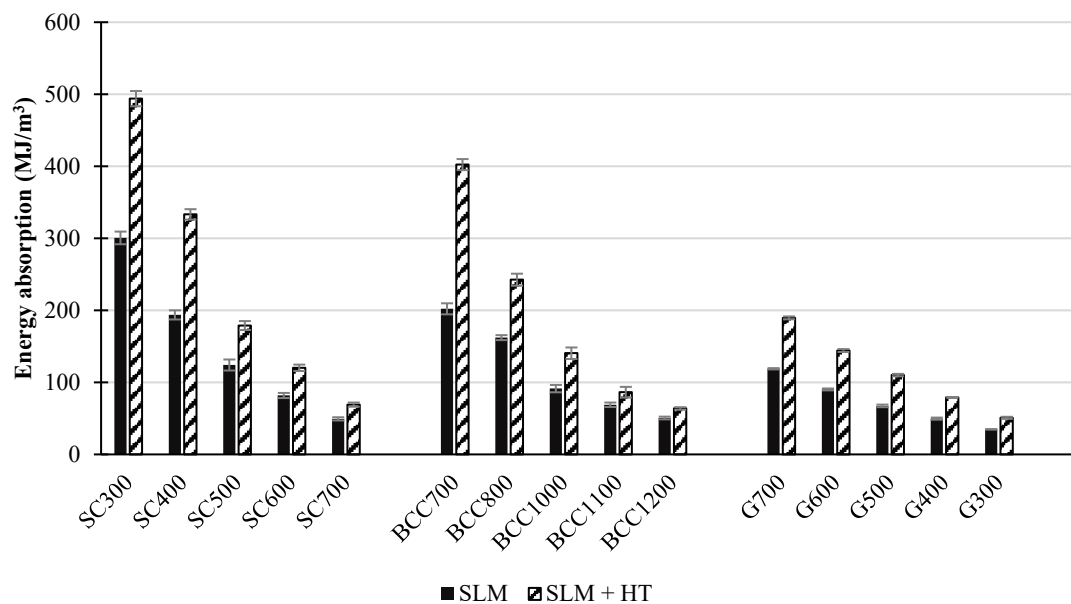

Figure 11. SC, BCC, and gyroid structures' energy absorption up to 0.5 strain.

Very different energy absorption values were also determined for the SC700 and BCC700 structures after heat treatment, namely 69.14 ($\pm$2.90) and 402.27 ($\pm$7.65) MJ/m^3, with a significant increase of 482% when comparing BCC with SC.

The gyroid structures displayed energy absorption between 34.79 ($\pm$0.32) and 118.87 ($\pm$0.89) MJ/m^3 (before heat treatment) and between 50.88 ($\pm$1.43) and 189.55 ($\pm$1.99) MJ/m^3 (after heat treatment). Increases in the strut dimension (T) led to increased absorbed energy as expected, with a 71% increase when comparing the as-produced G300 to G700. After heat treatment, this increase was approximately 73%.

Overall, the heat treatment improved the strut-based structures' energy absorption capacity by 52% on average, while regarding gyroids, this increase was 58% on average.

Finally, when comparing structures with different architectures and dimensions that possess similar porosity, it is possible to reach a conclusion on the load-bearing ability, stiffness, and energy absorption capacity of these different types of structures. By analyzing Table 6, it is possible to verify that SC600, BCC1200, and G500 have very similar experimental porosities, namely 68.14, 68.42, and 68.41%; however, when comparing these structures' first maximum compressive strength, quasi-elastic gradient, and energy absorption, it is possible to verify that the gyroid structures present much higher properties than the corresponding strut-based SC and BCC structures.

3.4. Permeability Testing

Figure 12 shows the experimentally determined permeability for the different structures and pressure differences that were applied as a function of their experimental porosity.

According to Darcy's law, the pressure differential and permeability are inversely proportional, and thus, the higher the pressure differential applied, the lower the permeability. This is generally verified for the three types of structures, for all dimensions, as seen in Figure 12. Overall, it is verified that higher porosities, due to larger pore sizes, led to higher permeability. In the case of the SC structures, permeability values between 4.9×10^{-11} ($\pm 1.4 \times 10^{-13}$) and 2.0×10^{-10} ($\pm 1.2 \times 10^{-12}$) m^2 were obtained, while for the BCC structures, this range was between 2.2×10^{-11} ($\pm 4.7 \times 10^{-13}$) and 1.2×10^{-10} ($\pm 5.4 \times 10^{-13}$) m^2, and, finally, for the gyroid structures, values from 6.7×10^{-11} ($\pm 1.2 \times 10^{-13}$) to 1.6×10^{-10} ($\pm 7.7 \times 10^{-13}$) m^2 were determined.
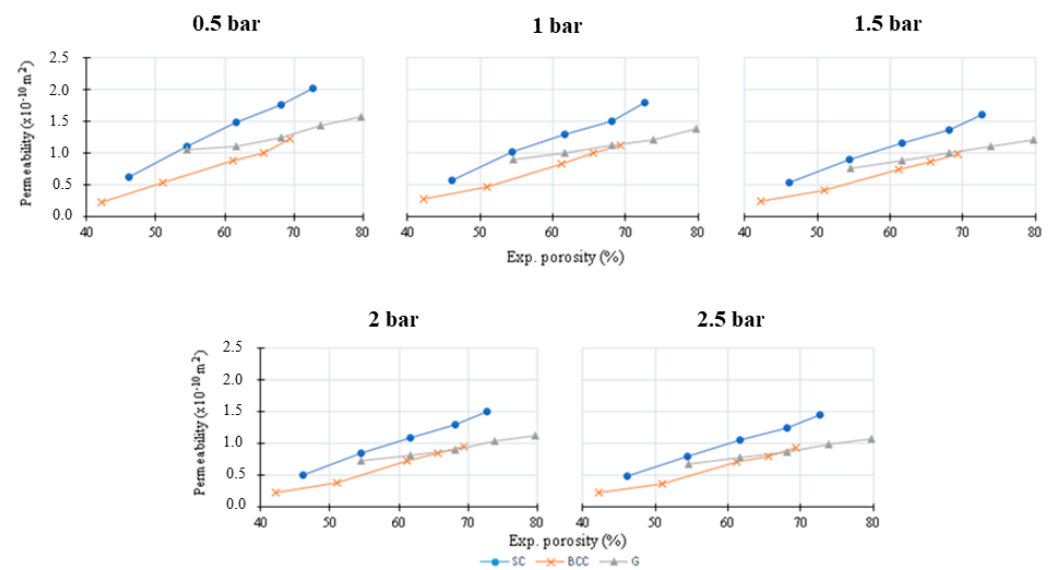
Figure 12. Permeability of SC, BCC, and gyroid structures.

When comparing the different lattice structures, it is possible to conclude that simple cubic (SC) structures consistently attained the highest permeability, regardless of the porosity, due to the fully open unit cell. When struts were added to the simple cubic unit cell, as in the BCC structures presented here, the permeability was hampered, and lower values than those obtained in SC were achieved.

The SC and BCC structures with the same unit cell dimensions showed a significant difference in permeability, with the highest values being consistently achieved when using SC for all the pressure differences tested. At 2.5 bar, SC700 (1.4×10^{-10} ($\pm 2.0 \times 10^{-13}$) m^2) displayed a 540% higher permeability than BCC700 (2.3×10^{-11} ($\pm 9.4 \times 10^{-14}$) m^2). For 2.0, 1.5, 1.0, and 0.5 bar, this difference was 543%, 539%, 542%, and 795%, respectively.

For intermediate porosity values, the BCC and gyroid structures were found to display similar permeability values, and in this sense, for a given range of gas permeability, a choice can be made between these two types of structures according to the required mechanical properties, which were previously assessed.

Overall, this study shows that structuring is a powerful tool to modify gas permeability, displaying adequate strength and stiffness for a given application, particularly for injection mold gas venting.

4. Conclusions

The following conclusions can be outlined from this study:

18Ni300 maraging steel lattice structures were successfully fabricated via SLM, and their mechanical performance and permeability were evaluated and compared.

The analysis of the SLM-fabricated lattice structures demonstrated small dimensional deviations from the CAD designs.

The produced structures' first maximum compressive strength, quasi-elastic gradient, and energy absorption were highly dependent on the architecture and were significantly improved after heat treatment.

Comparing the structures with similar porosity, the highest permeability was achieved by the SC structures, and the lowest was achieved by the BCC structures.

The obtained results can be used as tools for the design of AM porous vents for injection molding applications, with tailored permeability fit for a particular injection mold.

Author Contributions: Conceptualization, G.M., J.M.O. and J.S.V.; methodology, D.F.O. and J.S.V.; software, D.F.O.; validation, G.M., J.M.O. and J.S.V.; formal analysis, G.M. and D.F.O.; investigation, D.F.O., I.D. and G.V.; resources, G.M., J.M.O., I.D. and G.V.; data curation, G.M.; writing—original

References

1. Maconachie, T.; Leary, M.; Lozanovski, B.; Zhang, X.; Qian, M.; Faruque, O.; Brandt, M. SLM lattice structures: Properties, performance, applications and challenges. *Mater. Des.* **2019**, *183*, 108137. [CrossRef]
2. Babamiri, B.B.; Askari, H.; Hazeli, K. Deformation mechanisms and post-yielding behavior of additively manufactured lattice structures. *Mater. Des.* **2020**, *188*, 108443. [CrossRef]
3. Helou, M.; Kara, S. Design, analysis and manufacturing of lattice structures: An overview. *Int. J. Comput. Integr. Manuf.* **2018**, *31*, 243–261. [CrossRef]
4. Riva, L.; Ginestra, P.S.; Ceretti, E. Mechanical characterization and properties of laser-based powder bed-fused lattice structures: A review. *Int. J. Adv. Manuf. Technol.* **2021**, *113*, 649–671. [CrossRef]
5. Zadpoor, A.A. Mechanical performance of additively manufactured meta-biomaterials. *Acta Biomater.* **2019**, *85*, 41–59. [CrossRef] [PubMed]
6. Mahshid, R.; Hansen, H.N.; Højbjerre, K.L. Strength analysis and modeling of cellular lattice structures manufactured using selective laser melting for tooling applications. *Mater. Des.* **2016**, *104*, 276–283. [CrossRef]
7. Chouhan, G.; Gunji, B. Additive manufacturing TPMS lattice structures: Experimental study on airflow resistivity. *Results Mater.* **2023**, *20*, 100478. [CrossRef]
8. *ISO 17296-2:2015*; Additive Manufacturing—General Principles—Part 2: Overview of Process Categories and Feedstock. ISO: Geneva, Switzerland, 2015. Available online: https://www.iso.org/standard/61626.html (accessed on 5 February 2022).
9. Nouri, A.; Rohani Shirvan, A.; Li, Y.; Wen, C. Additive manufacturing of metallic and polymeric load-bearing biomaterials using laser powder bed fusion: A review. *J. Mater. Sci. Technol.* **2021**, *94*, 196–215. [CrossRef]
10. Sola, A.; Nouri, A. Microstructural porosity in additive manufacturing: The formation and detection of pores in metal parts fabricated by powder bed fusion. *J. Adv. Manuf. Process.* **2019**, *1*, e10021. [CrossRef]
11. Monroy, K.; Delgado, J.; Ciurana, J. Study of the pore formation on CoCrMo alloys by selective laser melting manufacturing process. *Procedia Eng.* **2013**, *63*, 361–369. [CrossRef]
12. Qi, D.; Yu, H.; Liu, M.; Huang, H.; Xu, S.; Xia, Y.; Qian, G.; Wu, W. Mechanical behaviors of SLM additive manufactured octet-truss and truncated-octahedron lattice structures with uniform and taper beams. *Int. J. Mech. Sci.* **2019**, *163*, 105091. [CrossRef]
13. Dallago, M.; Zanini, F.; Carmignato, S.; Pasini, D.; Benedetti, M. Effect of the geometrical defectiveness on the mechanical properties of SLM biomedical Ti6Al4V lattices. *Procedia Struct. Integr.* **2018**, *13*, 161–167. [CrossRef]
14. Yan, C.; Hao, L.; Hussein, A.; Raymont, D. Evaluations of cellular lattice structures manufactured using selective laser melting. *Int. J. Mach. Tools Manuf.* **2012**, *62*, 32–38. [CrossRef]
15. Giganto, S.; Martínez-Pellitero, S.; Barreiro, J.; Zapico, P. Influence of 17-4 PH stainless steel powder recycling on properties of SLM additive manufactured parts. *J. Mater. Res. Technol.* **2022**, *16*, 1647–1658. [CrossRef]
16. Wang, Y.; Guo, W.; Xie, Y.; Li, H.; Zeng, C.; Xu, M.; Zhang, H. In-situ monitoring plume, spattering behavior and revealing their relationship with melt flow in laser powder bed fusion of nickel-based superalloy. *J. Mater. Sci. Technol.* **2024**, *177*, 44–58. [CrossRef]
17. Takata, N.; Nishida, R.; Suzuki, A.; Kobashi, M.; Kato, M. Crystallographic features of microstructure in maraging steel fabricated by selective laser melting. *Metals* **2018**, *8*, 440. [CrossRef]
18. Laleh, M.; Sadeghi, E.; Revilla, R.I.; Chao, Q.; Haghdadi, N.; Hughes, A.E.; Xu, W.; De Graeve, I.; Qian, M.; Gibson, I.; et al. Heat treatment for metal additive manufacturing. *Prog. Mater. Sci.* **2023**, *133*, 101051. [CrossRef]

19. Dehgahi, S.; Sanjari, M.; Ghoncheh, M.H.; Shalchi Amirkhiz, B.; Mohammadi, M. Concurrent improvement of strength and ductility in heat-treated C300 maraging steels produced by laser powder bed fusion technique. *Addit. Manuf.* **2021**, *39*, 101847. [CrossRef]

20. Mutua, J.; Nakata, S.; Onda, T.; Chen, Z.C. Optimization of selective laser melting parameters and influence of post heat treatment on microstructure and mechanical properties of maraging steel. *Mater. Des.* **2018**, *139*, 486–497. [CrossRef]

21. Ferreira, D.F.S.; Miranda, G.; Oliveira, F.J.; Oliveira, J.M. Predictive models for an optimized fabrication of 18Ni300 maraging steel for moulding and tooling by Selective Laser Melting. *J. Manuf. Process.* **2021**, *70*, 46–54. [CrossRef]

22. Kučerová, L.; Zetková, I.; Jeníček, Š.; Burdová, K. Hybrid parts produced by deposition of 18Ni300 maraging steel via selective laser melting on forged and heat treated advanced high strength steel. *Addit. Manuf.* **2020**, *32*, 101108. [CrossRef]

23. Blakey-Milner, B.; Gradl, P.; Snedden, G.; Brooks, M.; Pitot, J.; Lopez, E.; Leary, M.; Berto, F.; du Plessis, A. Metal additive manufacturing in aerospace: A review. *Mater. Des.* **2021**, *209*, 110008. [CrossRef]

24. Guo, Y.; Yang, H.; Lin, G.; Jin, H.; Shen, X.; He, J.; Miao, J. Thermal performance of a 3D printed lattice-structure heat sink packaging phase change material. *Chin. J. Aeronaut.* **2021**, *34*, 373–385. [CrossRef]

25. Park, S.J.; Lee, J.H.; Yang, J.; Heogh, W.; Kang, D.; Yeon, S.M.; Kim, S.H.; Hong, S.; Son, Y.; Park, J. Lightweight injection mold using additively manufactured Ti-6Al-4V lattice structures. *J. Manuf. Process.* **2022**, *79*, 759–766. [CrossRef]

26. Timercan, A.; Sheremetyev, V.; Brailovski, V. Mechanical properties and fluid permeability of gyroid and diamond lattice structures for intervertebral devices: Functional requirements and comparative analysis. *Sci. Technol. Adv. Mater.* **2021**, *22*, 285–300. [CrossRef] [PubMed]

27. Ali, D.; Sen, S. Finite element analysis of mechanical behavior, permeability and fluid induced wall shear stress of high porosity scaffolds with gyroid and lattice-based architectures. *J. Mech. Behav. Biomed. Mater.* **2017**, *75*, 262–270. [CrossRef] [PubMed]

28. Ma, S.; Tang, Q.; Feng, Q.; Song, J.; Han, X.; Guo, F. Mechanical behaviours and mass transport properties of bone-mimicking scaffolds consisted of gyroid structures manufactured using selective laser melting. *J. Mech. Behav. Biomed. Mater.* **2019**, *93*, 158–169. [CrossRef]

29. Dhinakar, A.; Li, B.E.; Chang, Y.C.; Chiu, K.C.; Chen, J.K. Air permeability of maraging steel cellular parts made by selective laser melting. *Materials* **2021**, *14*, 3118. [CrossRef]

30. *ASTM B213-20*; Standard Test Methods for Flow Rate of Metal Powders Using the Hall Flowmeter Funnel. ASTM: West Conshohocken, PA, USA, 2020.

31. Maraging Steel M300 Powder for Additive Manufacturing. 2017. Available online: www.renishaw.com/additive (accessed on 20 November 2023).

32. Ferreira, D.F.S.; Vieira, J.S.; Rodrigues, S.P.; Miranda, G.; Oliveira, F.J.; Oliveira, J.M. Dry sliding wear and mechanical behaviour of selective laser melting processed 18Ni300 and H13 steels for moulds. *Wear* **2022**, *488–489*, 204179. [CrossRef]

33. *ISO 13314:2011*; Mechanical Testing of Metals—Ductility Testing—Compression Test for Porous and Cellular Metals. ISO: Geneva, Switzerland, 2011.

34. Król, M.; Snopiński, P.; Czech, A. The phase transitions in selective laser-melted 18-NI (300-grade) maraging steel. *J. Therm. Anal. Calorim.* **2020**, *142*, 1011–1018. [CrossRef]

35. Vishwakarma, J.; Chattopadhyay, K.; Santhi Srinivas, N.C. Effect of build orientation on microstructure and tensile behaviour of selectively laser melted M300 maraging steel. *Mater. Sci. Eng. A* **2020**, *798*, 140130. [CrossRef]

36. Guo, L.; Zhang, L.; Andersson, J.; Ojo, O. Additive manufacturing of 18% nickel maraging steels: Defect, structure and mechanical properties: A review. *J. Mater. Sci. Technol.* **2022**, *120*, 227–252. [CrossRef]

37. Bajaj, P.; Hariharan, A.; Kini, A.; Kürnsteiner, P.; Raabe, D.; Jägle, E.A. Steels in additive manufacturing: A review of their microstructure and properties. *Mater. Sci. Eng. A* **2020**, *772*, 138633. [CrossRef]

38. Bai, Y.; Wang, D.; Yang, Y.; Wang, H. Effect of heat treatment on the microstructure and mechanical properties of maraging steel by selective laser melting. *Mater. Sci. Eng. A* **2019**, *760*, 105–117. [CrossRef]

39. Chadha, K.; Tian, Y.; Bocher, P.; Spray, J.G.; Aranas, C. Microstructure evolution, mechanical properties and deformation behavior of an additively manufactured maraging steel. *Materials* **2020**, *13*, 2380. [CrossRef] [PubMed]

40. Chen, Y.; Liu, C.; Yan, H.; Fan, Y.; Wang, J.; Cui, Y. Effect of gas nitriding on 316 L stainless steel lattice manufactured via selective laser melting. *Surf. Coat. Technol.* **2022**, *441*, 128559. [CrossRef]

41. Kempen, K.; Yasa, E.; Thijs, L.; Kruth, J.P.; van Humbeeck, J. Microstructure and mechanical properties of selective laser melted 18Ni-300 steel. *Phys. Procedia* **2011**, *12*, 255–263. [CrossRef]